Development Processes of Extratropical Cyclones over the Korean Peninsula

한반도 근처 저기압의 발달 과정

2020 년 8 월

서울대학교 대학원

지구환경과학부

강 준 석

Abstract

The dynamical processes responsible for the rapid intensification of East Asian cyclones around the Korean Peninsula are quantitatively evaluated by inverting the potential vorticity (PV) tendency equation. The rapidly-intensifying cyclones, identified using the automated tracking algorithm, typically exhibit distinct northern or southern track when approaching the Korean Peninsula. The northern-track cyclones rapidly intensify mostly by zonal PV advection (103.5%) and latent heating process (29.0%). These processes also rapidly intensify the southern-track cyclones (72.1% and 56.0%, respectively) along with the vertical PV advection (19.5%). The negative contributions are made by meridional PV advection (~-25%) and the surface temperature tendency (-10%) for both cases. The difference in the development processes is analyzed by inverting the decomposed advection terms. The difference in the contribution of zonal PV advection is related to that in the upper-level trough axis. The extent of latent heating involved in the development affects the differing contribution of latent heat processes as well as the vertical PV advection.

Table of Contents

List of Figures

Figure 6. ξ_{850} from (a, b) reanalysis, (c,d) $-u\frac{\partial q_l}{\partial x}$, (e,f) $-v\frac{\partial q_l}{\partial y}$, (g,h) $-\omega\frac{\partial q_l}{\partial p}$, (i,j) Q_{LH}, and (k, l) $-\frac{R_d}{p}\left(\frac{\partial T}{\partial t}\right)_{BC}$ (shading, units: CVU 12 hr^{-1}) with respect to the center of NT and ST cyclones (red triangle) at t_{max}. The values that are statistically significant at the 95% confidence level, based on the Bootstrap resampling test, are dotted.

Figure 7. Area-averaged ξ_{850} for reanalysis, inversions and the sum of piecewise inversions for (a) NT and (b) ST cyclones. The relative contribution to observed ξ_{850} (leftmost bar) is denoted in percentage. The 95% confidence intervals, based on Bootstrap resampling test, are also shown.

Figure 8. Same as Fig. 7, but for decomposed advection terms.

Figure S1. Springtime (March–May) climatology of (a) LPV (shading, units: PVU) and (b) zonal wind (shading, units: m s^{-1}) at 250 hPa, and (c) integrated water vapor from 1000 to 250 hPa (shading, units: kg m^{-2}). In (a) the 2–PVU line is depicted in white as a reference.

Figure S2. Temperature tendency at 875 hPa (shading, units: K 12hr^{-1}) with respect to the center of (a) ST and (b) ST cyclones at t_{max}. The values that are statistically significant at the 95% confidence level, based on the Bootstrap resampling test, are dotted.

Figure S3. Same as Fig. 6 but for ξ_{850} from sum of piecewise inversions

1. Introduction

The extratropical cyclones (ETCs) are an integral part of midlatitude weather, for the precipitation and wind they accompany (Hawcroft et al., 2012). They occur preferentially in winter over the regions with a sharp sea surface temperature gradient, otherwise known as the stormtracks (Chang et al., 2002; Hoskins and Hodges 2002). In East Asia, however, ETCs are also frequently formed over the continents. The two remarked cyclogenesis regions are Mongolia and East China, which are respectively the leeside of the Altai-Sayan mountains and the downstream of the Tibetan Plateau (Adachi and Kimura 2007; Lee et al., 2019). These ETCs are most frequent in Northern Hemispheric spring (Lee et al., 2019), suggesting that surface temperature gradient may not be the sole factor for their intensification.

The intensification processes of these continental cyclones are scrutinized in the potential vorticity perspective (Hoskins et al., 1985) in Kang et al. (2020) (hereafter referred to as K20). In the PV perspective, an ETC intensification is explained commonly by the circulations induced respectively by the upper- and lower-tropospheric PV anomalies and the potential temperature anomalies at the surface. Among the three, the first two anomalies are notable for the development of East Asian ETCs (K20). The upper-tropospheric PV anomalies are responsible for the intensification of the ETCs from Mongolia. The lower-tropospheric PV is only strengthened after the maximum development of the ETC, indicating that development of these cyclones are led by the enhanced upper-level trough. On the other hand, the development of the ETCs from

1

East China is mostly related to the latent heating (LH) process in their incipient stages, exhibiting strong lower-tropospheric PV anomalies (Stoelinga, 1996). However, during the maximum development, they are also affected by enhanced positive PV anomalies in the upper troposphere.

Though the development processes of these two groups of ETCs are documented in detail in K20, further quantitative analysis in the PV perspective is required. Such quantification can be performed by PV inversion calculations (Davis and Emanuel 1991; Davis, 1992). The circulation associated with each PV anomaly is calculated through PV inversion when provided with boundary conditions. However, the PV inversion is a diagnostic analysis and implicitly evaluates the ETC developing processes. For instance, the PV inversion regards the lower-tropospheric PV as indicative of the LH process (Seiler, 2019), while in fact, PV is produced below the level of maximum LH prognostically. In this regard, modification to PV inversion in prognostic perspective is motivated.

In this study, the development of East Asian cyclones around the Korean Peninsula is examined quantitatively as an extension of K20. The ETCs analyzed in this study are identical to those in K20, which were achieved by utilizing the automated tracking algorithm to the vorticity field during 1979-2017. A processes-based prognostic PV inversion, which is a method newly devised in this study, is carried out for each ETC. This method calculates the circulation change from PV-changing processes. Then, the vorticity tendencies retrieved from respective processes are evaluated.

The rest of the paper is organized as follows. Section 2 describes the data and ETC tracking and sampling. The PV tendency

2

inversion is explained in detail in section 3. Characteristics of the developing cyclones are briefly explored in section 4, followed by the quantitative investigation in section 5. The final section is devoted to summary and discussion.

2. Data and Methods

2.1 Data

In this study, the 6-hourly ERA-Interim reanalysis data (Dee et al., 2011) is utilized. Specifically, relative vorticity, geopotential, temperature, horizontal winds, pressure velocity, and specific humidity interpolated onto 1.5°×1.5° horizontal grids and 37 isobaric levels are used. The PV and its linearized form are calculated from these variables through second-order finite difference method, where $\partial x \approx \Delta x = R_e \Delta \lambda \cos \varphi$ and $\partial y \approx \Delta y = R_e \Delta \varphi$. Here, R_e is the Earth's radius and $\Delta \lambda$ and $\Delta \varphi$ are zonal and meridional grid spacings in the reanalysis data.

2.2 ETC tracking and sampling

The same ETCs analyzed in K20 are also used in this study. The ETC tracks are achieved utilizing the automated feature tracking algorithm (Hodges, 1994, 1995, 1999) to the 850-hPa relative vorticity data during 1979–2017. The algorithm detects and tracks local maxima of relative vorticity, which are regarded as ETC tracks. Focusing on the synoptic scale, the vorticity field of horizontal wavenumber 5 to 42 is used. The short-lived and quasi-stationary ETCs are excluded by considering the cyclones that last more than 48 hours and travel further than 1000 km. Tropical cyclones are removed from the track data by excluding the cyclones that are generated below 25ºN (see also Lee et al., 2019 for further details of tracking method).

In K20, the ETCs passing the Korean Peninsula are selected

and classified. The intensifying ETCs traveling through the region between 120°–135°E and 33°–48°N (blue box in Fig. 1) are chosen. Since these ETCs have two distinguished origins (see also Fig. 1 in K20), they are further categorized into two groups, using the fuzzy c means clustering method (Bezdek et al., 1984). The ETCs originating from Mongolia are set as the northern-track (NT) cyclones, and those from East China are termed as the southern-track (ST) cyclones. There are 1204 NT cyclones and 1214 ST cyclones detected during the 39 years (1979–2017).

For all ETCs, the intensification rate at time step t, IR(t), is defined as below from the twelve-hour difference of filtered 850-hPa relative vorticity.

$$\text{IR}(t) = \zeta(t + 6hrs) - \zeta(t - 6hrs) \tag{1}$$

The maximum intensification rate within the domain (IR_{max}) and the corresponding time step t_{max} is defined for each ETC. To focus on ETCs that intensify rapidly, the ETCs with the top 10% of IR_{max} are primarily selected for analysis. There are more ST than NT cyclones (144 to 97) in this strong sample, hinting that ST cyclones tend to develop more intense than their counterparts (K20).

3. Inversion of the PV Tendency Equation

This section introduces the new method that calculates the circulation change induced from processes that change PV anomaly distribution.

3.1 Linearized PV

The PV (Ertel, 1942), q, on isobaric surface is expressed as follows.

$$q = -g(f + \zeta)\frac{\partial \theta}{\partial p} + g\left(\frac{\partial v}{\partial p}\frac{\partial \theta}{\partial x} - \frac{\partial u}{\partial p}\frac{\partial \theta}{\partial y}\right). \qquad (2)$$

Here, g is the gravitational acceleration, f is the planetary vorticity, $\zeta = \frac{\partial v}{\partial x} - \frac{\partial u}{\partial y}$ is the relative vorticity, u and v are the zonal and meridional winds, and θ is the potential temperature. From Eq. (2) and the balance state of Charney (1955), horizontal wind and potential temperature from a specific PV anomaly can be retrieved (Davis, 1992). This technic is particularly useful since it quantifies the intensity of the circulation induced by a PV anomaly (Seiler, 2019).

The PV is conserved within a frictionless−adiabatic flow, and the following equation holds for the change of PV over time.

$$\frac{\partial q}{\partial t} = -\mathbf{u} \cdot \nabla_p q + Q + F \qquad (3)$$

Here, $\mathbf{u} = (u, v, \omega)$ is the three−dimensional wind vector, $\nabla_p = \left(\frac{\partial}{\partial x}, \frac{\partial}{\partial y}, \frac{\partial}{\partial p}\right)$, Q and F are the PV changes from diabatic heating and horizontal friction. The physical processes related to ETC development can be explained by the rhs of Eq. (3). The horizontal

6

advections represent the migration ETC, nonlinear interactions in the vertical, or wave propagation (Nielsen−Gammon and Lefevre 1996). The non−conservative term, Q, is important since it includes the effect of LH.

Then, how do the wind and temperature change for each PV− changing process? For instance, in an ETC, how much does the wind intensify from Q? Since Q would change both wind and temperature, the extent of respective changes are not separable without additional equations. To provide an answer, the PV is linearized with some assumptions, including the quasi−geostrophic (QG) approximation (Charney and Stern 1962). The linearized PV (LPV), q_L, is formulated as

$$q_L = -g \frac{\partial \bar{\theta}}{\partial p} \left(\frac{1}{f_0} \nabla^2 \phi + f + \frac{f}{\sigma} \frac{\partial^2 \phi'}{\partial p^2} \right), \tag{4}$$

where f_0 is the planetary vorticity at the center of each EC, $\nabla = (\frac{\partial}{\partial x}, \frac{\partial}{\partial y}, 0)$ is the horizontal gradient operator, ϕ is the geopotential, $\sigma = -\frac{R_d \pi}{p} \frac{\partial \bar{\theta}}{\partial p}$, R_d is the gas constant of dry air, $\pi = \left(\frac{p}{p_s} \right)^{\frac{R_d}{c_p}}$ is the Exner function, c_p is the specific heat of dry air under constant pressure, and $p_s = 1000$ hPa. The overbar denotes monthly climatology, while the prime represents the corresponding anomaly. Then, the anomalous component of LPV becomes

$$q_L' = \mathrm{L}(\phi').$$

Here, $\mathrm{L} \equiv -g \frac{\partial \bar{\theta}}{\partial p} \left(\frac{1}{f_0} \nabla^2 + \frac{f}{\sigma} \frac{\partial^2}{\partial p^2} \right)$ is the linear function that calculates LPV anomaly from a geopotential anomaly. The nonlinear PV in Eq. (2) and the LPV in Eq. (4) is quantitatively similar when dealing with multiple composites of ETCs.

3.2 Application of the PV tendency equation

Owing to the similarity between the PV and LPV (i.e., $q \approx q_l$), q is substituted with q_l in Eq. (3) as follows.

$$\mathrm{L}(\chi) = -u\frac{\partial q_L}{\partial x} - v\frac{\partial q_L}{\partial y} - \omega\frac{\partial q_L}{\partial p} + Q_{LH} + F_{RES} \qquad (5)$$

Note that $\frac{\partial q_L}{\partial t} = \mathrm{L}\left(\frac{\partial \phi'}{\partial t}\right) = \mathrm{L}(\chi)$, where $\chi \equiv \frac{\partial \phi}{\partial t}$ is the geopotential tendency. The meanings of Q_{LH} and F_{RES} is described in the following paragraph. From Eq. (5), it follows that,

$$\chi = \mathrm{L}^{-1}\left(-u\frac{\partial q_L}{\partial x}\right) + \mathrm{L}^{-1}\left(-v\frac{\partial q_L}{\partial y}\right) + \mathrm{L}^{-1}\left(-\omega\frac{\partial q_L}{\partial p}\right) + \mathrm{L}^{-1}(Q_{LH}) + \mathrm{L}^{-1}(F_{RES}) \qquad (6)$$
$$+ \chi_{BC}.$$

This indicates that with proper boundary conditions (χ_{BC}), the geopotential tendency can be calculated with the sum of the piecewise inversion of the terms on the rhs of Eq. (5). It also means that the change of geopotential from each term on the rhs of Eq. (5) is achievable.

To exclusively consider the effect of LH, the LPV change from diabatic heating in Eq. (3) is decomposed into that from LH and the residual heating, i.e., $Q = Q_{LH} + Q_{RES}$. The PV change from LH is formulated as

$$Q_{LH} = -g(f + \zeta)\frac{\partial \dot{\theta}_{LH}}{\partial p},$$

following Tamarin and Kaspi (2016), and the LH ($\dot{\theta}_{LH}$) is calculated as below (Emanuel et al., 1987).

$$\dot{\theta}_{LH} = \omega\left(\frac{\partial \theta}{\partial p} - \frac{\gamma_m}{\gamma_d}\frac{\theta}{\theta_e}\frac{\partial \theta_e}{\partial p}\right)$$

Here, θ_e is the equivalent potential temperature, and γ_d and γ_m are dry and moist adiabatic lapse rates, respectively. Accordingly, $F_{RES} =$

$Q_{RES} + F$, is the sum of PV change from residual heating and friction.

3.3. Devising the inversion calculations

For the inversion shown in Eq. (6), boundary conditions are necessary. While the inversion is carried out in a cubic domain about the center of each ETC, homogeneous Dirichlet boundary condition ($\chi = 0$) is used at the lateral boundaries ($\pm 30^{\circ}$E, $\pm 15^{\circ}$N from the domain center). In the top and bottom boundaries, the either homogeneous or nonhomogeneous Neumann boundary condition is applied. The nonhomogeneous Neumann boundary condition, which acts as a separate PV tendency at the surfaces (Bretherton, 1966), is formulated as below.

$$\left(\frac{\partial \chi}{\partial p}\right)_{BC} = -\frac{R_d}{p}\left(\frac{\partial T}{\partial t}\right)_{BC} \tag{7}$$

Here, the subscript BC denotes that this condition is applied at the top and bottom boundaries, which are 175 and 875 hPa, respectively. For inversions with nonhomogeneous Neumann condition, the rhs of Eq. (7) is set to zero. Note that analogous to positive potential temperature anomaly in PV inversion, the positive temperature tendency at the surface increases cyclonic rotation in the levels above.

The inversion described in this section is applied to both NT and ST cyclones at their t_{max}. Six inversions are performed for each cyclone. The five inversions have the five terms in the rhs of Eq. (5) as interior PV tendency forcing, with homogeneous Neumann condition applied at the top and bottom boundaries. The last inversion has zero interior PV tendency forcing, but instead have nonhomogeneous condition applied, closing the linear set of

inversions.

The resulting geopotential tendencies from the inversions are further quantified and evaluated in terms of the geostrophic vorticity tendency at 850 hPa (ξ_{850}), which is defined as below.

$$\xi_{850} \equiv \frac{\partial \zeta_{g,850}}{\partial t} = \frac{1}{f_0} \nabla^2 \chi_{850}$$

Here, the subscript 850 indicates that the values are calculated from the geopotential tendency at 850 hPa.

4. Characteristics of ETCs

Prior to performing inversion calculations, the developmental characteristics of the NT and ST cyclones are briefly discussed. At the same time, the use of the method described in the previous section is validated.

Figure 1 illustrates the track frequency of the sampled ETCs. As introduced earlier, the NT cyclones typically initiate from Mongolia and pass the northern part of the Korean peninsula (Fig. 1a), and the ST cyclones are mostly generated in East China (Fig. 1b). Note that the numbers represent only the sampled cyclones and do not indicate the total number of ETCs passing the region. Since both NT and ST cyclones are most frequent in spring (March–May; see also Fig. 4 in K20), only springtime ETCs, with respect to the date of t_{max}, are further analyzed. This results in a total of 36 NT and 65 ST cyclones. Hereafter, the NT and ST cyclones refer to this springtime strong sample unless noted otherwise.

Our method quantifies the ETC development using the geostrophic vorticity at 850 hPa. In this regard, it should be validated whether the time evolution of the 850−hPa geostrophic vorticity coincides with the intensity and IR, which are defined in section 2 by the filtered relative vorticity at 850−hPa.

The time evolution of geostrophic vorticity and IR_g is depicted in Fig. 2. Here, the shown geostrophic vorticity represents the maximum 850−hPa geostrophic vorticity within $6^{\circ} \times 6^{\circ}$ box about the ETC center at each time step. The intensification rate of this geostrophic vorticity (IR_g) is defined by substituting the filtered

vorticity into geostrophic vorticity in Eq. (1). For both NT and ST cyclones, IR_g peaks at t_{max}, indicating that geostrophic vorticity could be indicative of rapid intensification processes (Yoshida and Asuma, 2004). Apart from this similarity, the ST cyclones exhibit maximum IR_g about 6.9 CVU $12hr^{-1}$ (1 CVU = 10^{-5} s^{-1}), which is larger than that of the NT cyclones (6.0 CVU $12hr^{-1}$). This is consistent with K20, which also reported that stronger IR_{max} is found from the ST cyclones compared to the NT cyclones (see their Fig. 2). Besides, while the IR_g of the ST cyclones has a single peak at t_{max}, the IR_g at t_{max} and six hours after are very close for NT cyclones.

It is well known that strong ETC intensification is associated with increased PV from the near−surface to the tropopause (Wang and Rogers, 2001). This structure, expectedly, is found in the selected ETCs. Figure 3a illustrates the vertical cross−section of PV, where the vertical cross−section is made with the average of values in the 15° latitude band about the ETC center. While the PV is climatologically higher with increasing height, PV over 1 PVU (1 PVU = 10^{-6} K m^2 kg^{-1} s^{-1}) intrudes down to 400 hPa, indicating that these cyclones are in general, related to the enhanced upper−tropospheric trough at t_{max}. Near the cyclone center in the lower−troposphere, PV over 0.6 PVU is observed, which is more than twice its surrounding values.

This vertical structure of PV or the 'PV tower' is also found in the vertical cross−section of LPV (Fig. 3b). Though LPV is slightly stronger than PV in the mid−to−upper troposphere, the overall structure is comparable, both qualitatively and quantitatively. The similarity of PV and LPV shown in Fig. 3 justifies the use of LPV in the analysis, and further suggests that the essences of the circulation

related to the analyzed ETCs are also retained in LPV.

The upper- and lower-tropospheric structures of LPV is further investigated for both NT and ST cyclones (Fig. 4). Figure 4a shows the upper-tropospheric LPV anomalies of NT cyclones. Noting that LPV is analogous to PV and is negatively proportional to geopotential (e.g., Eq. (4)), stronger upper-level trough is observed for NT cyclones west to the cyclone center as in K20. The maximum of the LPV anomalies is about 3.0 PVU, and the trough axis directs eastwards from south to north. Accordingly, the anomalous wind is southwesterly above the center of NT cyclones at 250 hPa. On the other hand, the trough exhibits LPV anomalies about 2.0 PVU near the maximum, which is weaker than that of NT cyclones (Fig. 4b). The axis of the trough also is different, where it directs westwards from south to north, which is responsible for the southerly over the cyclone center. In the lower troposphere, weak LPV anomalies about 0.20 PVU is found for NT cyclones, whereas they are about 0.50 PVU for ST cyclones (Figs. 4c and d). The results shown in Fig. 4 greatly resembles Fig. 7 and 11 of K20, again validating the use of LPV in place of PV.

5. Quantitative Aspects of ETCs

5.1 PV tendency budgets

Figures 5a and b illustrate the vertical cross-section of $L(\chi)$, i.e., the LPV tendency, at t_{max} for NT and ST cyclones, respectively. The vertical cross-section is obtained from the same latitude band used in Fig. 3. In both figures, an eastward migration of a "PV tower" is found. At 850 hPa, the center of positive LPV tendency, which is the approximate location of the cyclone at the next time step, is located about 4.5° east from the cyclone center. The positive LPV tendency at the mid-to upper-troposphere is mostly associated with the zonal advection of LPV (Figs. 5c and d). However, unlike the LPV anomalies shown in Figs. 4a and b, the zonal advection is stronger for ST cyclones (~8 PVU $12hr^{-1}$) than for NT cyclones (~5 PVU $12hr^{-1}$). Apart from the fact that the strength of the anomaly does not follow that of its gradient, the discrepancy mostly is from the difference in the zonal wind. The ST cyclones, which are typically located more south than the NT cyclones at t_{max} (Fig. 1), develop below stronger upper-tropospheric zonal wind (Fig. S1b).

The meridional LPV advection is responsible for the negative tendency from the surface to tropopause above the cyclone center (Figs. 5e and f), partly offsetting the positive tendency from the zonal advection. In Figs. 5g and h, the vertical LPV advection produces a positive tendency in the mid to lower troposphere and induces negative tendency in the upper troposphere. However, it should be noted that the signs are sensitive to the choice of latitude band used in averaging, since vertical motions are narrow and slantwise. The

14

LPV change from LH dominates the tendency in the lower troposphere, particularly for ST cyclones. (Figs. 5i and j). A dipole of LPV tendency is also found about the level of maximum latent heating (600–700 hPa, see Figs. 6 and 10 in K20).

5.2 Inversion results

Figures 6a and b show the ξ_{850} from the reanalysis for NT and ST cyclones, respectively. In both figures, the maximum tendencies are observed at about 4° east from the center, while that of ST cyclones (Fig. 6b) is found more poleward than that of NT cyclones (Fig. 6a). The ξ_{850} of ST cyclones (10.0 CVU 12hr^{-1}) is slightly stronger than that of NT cyclones (9.7 CVU 12hr^{-1}). The ξ_{850} from zonal LPV advection (10.6 CVU 12hr^{-1}) is particularly in–phase with the observed positive ξ_{850} of NT cyclones (compare Figs. 6a and c). This implies that the strengthening of NT cyclones is largely influenced by zonal LPV advection. For ST cyclones, however, the ξ_{850} from zonal LPV advection is strong southeast of the center (Fig. 6d), and is small where the observed ξ_{850} is strong.

The meridional LPV advection induces negative ξ_{850} east to the center of both NT and ST cyclones (Figs. 6e and f), while small positive ξ_{850} is found at the northeast of the center for ST cyclones. The vertical LPV advection, hinders the development of NT cyclones, by bringing negative ξ_{850} near the center (Fig. 6g). However, it is the opposite for ST cyclones, where they are intensified by the ξ_{850} induced from the vertical advection (Fig. 6h). Owing to strong LH, positive ξ_{850} from Q_{LH} is about 4.9 CVU 12hr^{-1} for ST cyclones (Fig. 6j). The positive tendency from is Q_{LH} weaker for NT cyclones (3.0 CVU 12hr^{-1}, Fig. 6i), indicating that LH processes contribute lesser

to their development. Finally, the ξ_{850} from $-\frac{R_d}{p}\left(\frac{\partial T}{\partial t}\right)_{BC}$ is shown in Figs. 6k and l. Negative tendency is conspicuous near the center for both NT and ST cyclones, and the tendency has an eastward−accelerated phase compared to the observed ξ_{850} (compare Figs. 6a and k, 6b and l). This shifted tendency is coherent with the tendency found in the 875−hPa temperature (Fig. S2). It should also be noted that the sum of the piecewise inversions, including F_{RES} (not shown), are greatly close to the observed ξ_{850} (Fig. S3).

To better quantify the results, area−averaged ξ_{850} is used. For all ETCs, the maximum of ξ_{850} is sought from reanalysis (e.g., yellow X in Fig. 6a). Then, the ξ_{850} is averaged, within a $6°\times6°$ box centered on that maximum, for reanalysis, all inversions, and the sum of inversions. Additionally, the relative contributions of each term on rhs of Eq. (5) is measured as the ratio of ξ_{850} from inversion to the observed ξ_{850}.

The area−averaged ξ_{850} are shown in Fig. 7, where the relative contributions are denoted in percentage. For brevity, ξ_{850} stands for the area−averaged ξ_{850} in the rest of this section. The observed ξ_{850} for NT cyclones are about 6.2 CVU 12hr^{-1} (blue; Fig. 7a), and the zonal LPV advection (red) contributes 103.5% (6.4 CVU 12hr^{-1}) of this value. This clearly indicates that the NT cyclones are intensified through zonal PV advection associated with the upper−level trough (Fig. 5c). The NT cyclones are strengthened by Q_{LH} (cyan) to a smaller extent of about 29.0% (1.8 CVU 12hr^{-1}). The meridional advection (green) negatively contributes to the development of NT cyclones by −25.4% (−1.6 CVU 12hr^{-1}). The vertical advection (dark yellow) and temperature tendency at the surface (magenta) also hinder the intensification by −10.3% (−0.63

CVU 12hr^{-1}) and -10.9% (-0.67 CVU 12hr^{-1}), respectively. The F_{RES} (gray) shows small positive contribution, however, it is not statistically significant. The sum of piecewise inversions (dashed blue) underestimates the observed ξ_{850} by 5.5%, which represents the ability of our method in diagnosing NT cyclones.

The intensification processes of ST cyclones are quantified in Fig. 7b. The observed ξ_{850} is about 6.6 CVU 12hr^{-1} (blue), which is slightly stronger than NT cyclones. The relative contribution from zonal LPV advection (red) is about 72.1% (4.8 CVU 12hr^{-1}). Second to this process, the ξ_{850} from Q_{LH} (cyan) is 3.7 CVU 12hr^{-1} (56.0%), showing a strong contribution to the development. The ST cyclones are also strengthened by vertical LPV advection (dark yellow) by 19.5% (1.3 CVU 12hr^{-1}). The meridional advection (green) and temperature tendency at the surface (magenta) weaken the cyclone by -26.4% (-1.8 CVU 12hr^{-1}) and -9.3% (-0.6 CVU 12hr^{-1}), respectively. Negative contribution is also made from F_{RES}. Considering the sum of piecewise inversions (dashed blue), our method only misses the observed ξ_{850} of ST cyclones by 0.1%.

Comparing NT and ST cyclones with noting that their observed ξ_{850} are close, a distinct difference is found between the contributions of Q_{LH} (cyan). This difference is clearly from that in LH (see also Figs. 6 and 10 in K20), which is stronger in ST cyclones due to their adjacency to moisture source (Fig S1c). However, there are differences that their reasons are not as apparent. For instance, the signs of contribution from vertical LPV advection (dark yellow) are different between the two, but the reason for this difference is not hinted from Figs. 5g and h. Furthermore, the contribution from vertical advection is not statistically significant for NT cyclones

(dark yellow; Fig 7a), implying the possibility of cancellation between the terms consisting $-\omega\frac{\partial q_l}{\partial p}$. The contribution from zonal advection is larger in NT than in ST cyclones in terms of both absolute and relative value. This is, however, inconsistent with the zonal advection shown in Figs. 5c and d, where it was stronger in ST cyclones. As such, additional analyses are required to fully explain the developmental differences between the two groups of cyclones.

5.3 Decomposition of the advection terms

To better explain these aspects, further decomposition of the advection terms is made to Eq. (5) as follows.

$$\mathrm{L}(\chi) = -\overline{u}\frac{\partial q_l}{\partial x} - u'\frac{\partial q_l}{\partial x} - v\frac{\partial \overline{q_l}}{\partial y} - v\frac{\partial q_l'}{\partial y} - \omega\frac{\partial \overline{q_l}}{\partial p} - \omega\frac{\partial q_l'}{\partial p} + Q_{LH} + F_{RES} \tag{8}$$

As in section 3, the overbars denote monthly climatology and the primes are the corresponding anomalies. The zonal PV gradient, meridional wind, and pressure velocity are not decomposed, because their mean components are negligible compared to the anomalies. The decomposed advection terms in Eq. (8) are also inverted with homogeneous boundary conditions. The ξ_{850} from these inversions are shown in Fig. 8. The horizontal advections, in particular, are further divided into upper- and lower-tropospheric portions across 600 hPa.

The ξ_{850} from zonal LPV advection by mean wind (brown) represents the propagation of the cyclone and upper-level trough. It has the strongest influence on the intensification among the horizontal advection terms, for both NT and ST cyclones (81.0% and 86.5%, respectively). The zonal LPV advection by the upper-level mean flow has a greater influence than that from the lower-level.

The difference in the mean zonal wind (Fig. S1b) makes ξ_{850} from this term stronger for ST cyclones compared to NT cyclones. The difference of ξ_{850} from zonal advection (red in Figs.7a and b) comes from nonlinear zonal advections (pink). The nonlinear zonal advection intensifies NT cyclones, whereas it weakens ST cyclones. In NT cyclones, anomalous westerly advects positive LPV over east of the cyclone center (Fig 4a). However, anomalous easterly advects negative LPV anomaly to the east of the center of ST cyclones (Fig 4b). Considering that the anomalous winds are almost parallel to geopotential anomalies, the direction of the trough's axis affects the development of the ETCs, which is represented in the nonlinear zonal advection.

The meridional advections (dark green and olive) induce negative ξ_{850} for both NT and ST cyclones, except for the ξ_{850} from the lower-level LPV advection along the mean gradient for ST cyclones (right olive in Fig 8b). This is likely due to the local reversal of mean LPV around 33°N (not shown). The mean vertical advection introduces low LPV to the developing cyclone and weakens their intensification. However, at the same time, positive anomalies produced in the lower troposphere from the LH process are advected to the developing cyclone, inducing positive ξ_{850}. The vertical advection of mean LPV weakens the cyclone to a similar extent (orange, ~-3 CVU $12hr^{-1}$) for both NT and ST cyclones. However, the extents of the anomalous vertical advection are different. The anomalous vertical advection strengthens NT cyclones only by 2.5 CVU $12hr^{-1}$, whereas it intensifies the ST cyclones by 4.4 CVU $12hr^{-1}$. The anomalous LPV produced in the lower level is strong enough to overwhelm the climatological LPV stratification in the case of ST

cyclones. Note that the anomalous LPV in the lower level at t_{max} is the result of the LH in the preceding stages.

6. Summary and Discussion

In this study, the developing cyclones around the Korean Peninsula, which were qualitatively investigated in K20, is quantitatively analyzed. By approximating the PV into linearized form, the geostrophic vorticity tendency from each term in the PV tendency equation is calculated. The tendency of geostrophic vorticity is considered as a measure of cyclone intensification. The inverted vorticity tendency is compared to that from the observation to quantify their contribution.

The NT cyclones intensify mostly by zonal LPV advection (103.5%), followed by the LH process (26.0%). The meridional and vertical advections and the temperature tendency at the surface have negative effects on the intensification. The ST cyclones strengthen by zonal LPV advection (72.1%) and LH process (56.0%). They are also intensified by vertical advection (19.5%), and weakened by meridional advections and the temperature tendency at the surface.

Through the quantification, the difference in the development between NT and ST cyclones are explicitly analyzed. The reason for the difference in the contribution of zonal LPV advection is associated with zonal advection by the anomalous wind. The upper-level trough of NT cyclones induces westerlies over east of the cyclone center, promoting LPV increase over in the region. In contrast, the upper-level trough of ST cyclones brings negative LPV tendency to the east of cyclones. This difference is related to that in the direction of the trough axis. While the large contribution of the LH process is characterized in ST cyclones, this leads to the difference in the influence of vertical LPV advection. Since LPV produced from LH is

strong in ST cyclones, the vertical advection of LPV anomaly overwhelms the effect of LPV stratification. This results in the positive contribution of vertical LPV advection, which is the opposite for NT cyclones.

The result of this study suggests that the method of this study can be used to evaluate various factors affecting ETC development. The rapid ETC development often accompanies Rossby wave breaking (Gómara et al., 2014). The type of wave breaking, which could be related to the direction of the PV streamer, and the associated mechanism for ETC intensification can be explored with the method of our study. When inferring from our results, anticyclonic wave breaking would foster ETC intensification than its cyclonic counterpart, in terms of zonal LPV advection.

In K20, the resemblance of ST cyclones to diabatic Rossby waves (Boettcher and Wernli 2013) has been referred. The self-propagating characteristic of the diabatic Rossby waves is insinuated from the anomalous vertical advection of LPV in ST cyclones. In the case when lower-tropospheric LPV anomaly is weak (e.g., NT cyclones), vertical motions would not only enhance ETC intensity by LH release but also weaken it by bringing climatologically-low LPV air into the developing region. However, when the anomalous LPV is strong enough in the lower troposphere to overcome the LPV stratification, the vertical motions bring anomalously-strong LPV air into the developing region. Thus, the development is not countered, allowing for positive feedbacks.

The warm temperature anomaly at surface promotes cyclonic circulation in the troposphere, and therefore accounts for a significant amount of ETC intensity (Seiler, 2019). Nevertheless, the results of

this study indicate that they could be a negative factor for ETC development, when its tendency is not in-phase with that of the cyclone (Fig. S2).

It should be noted here that the use of Eq. (5) does not mean that LPV is conserved as PV in Eq. (3). It implies that for a given location and time $(\mathbf{x}, t)$, q and q_l are fairly similar, i.e., $q(\mathbf{x_1}, t_1) \approx q_l(\mathbf{x_1}, t_1)$, $q(\mathbf{x_2}, t_2) \approx q_l(\mathbf{x_2}, t_2)$, so that $\frac{Dq}{Dt} \approx \frac{Dq_l}{Dt}$ holds within tolerable accuracy. Although it is helpful to consider LPV as PV in the results, the difference between the two variables should always be concerned. Since caveats exist regarding the physical meanings of the terms in Eqs. (5) and (8), the numbers presented in this study should not be interpreted as absolute values from physical processes. Instead, emphasis should be put on the quantitative difference in developing processes of NT and ST cyclones. Further improvements to the presented method can be made when the implicitly expressed non-conservative processes (F_{RES}) are explicitly evaluated.

7. References

Adachi, S., & Kimura, F. (2007). A 36-year climatology of surface cyclogenesis in East Asia using high-resolution reanalysis data. *Sola*, *3*, 113-116.

Bezdek, J. C., Ehrlich, R., & Full, W. (1984). FCM: The fuzzy c-means clustering algorithm. *Computers & Geosciences*, *10*(2-3), 191-203.

Boettcher, M., & Wernli, H. (2013). A 10-yr climatology of diabatic Rossby waves in the Northern Hemisphere. *Monthly Weather Review*, *141*(3), 1139-1154.

Chang, E. K., Lee, S., & Swanson, K. L. (2002). Storm track dynamics. *Journal of Climate*, *15*(16), 2163-2183.

Charney, J. (1955). The use of the primitive equations of motion in numerical prediction. *Tellus*, *7*(1), 22-26.

Charney, J. G., & Stern, M. E. (1962). On the stability of internal baroclinic jets in a rotating atmosphere. *Journal of the Atmospheric Sciences*, *19*(2), 159-172.

Davis, C. A. (1992). Piecewise potential vorticity inversion. *Journal of the Atmospheric Sciences*, *49*(16), 1397-1411.

Dee, D. P., Uppala, S. M., Simmons, A. J., Berrisford, P., Poli, P., Kobayashi, S., et al. (2011). The ERA-Interim reanalysis: configuration and performance of the data assimilation system. *Quarterly Journal of the Royal Meteorological Society*, *137*(656), 553-597.

Emanuel, K. A., Fantini, M., & Thorpe, A. J. (1987). Baroclinic instability in an environment of small stability to slantwise

moist convection. Part I: Two-dimensional models. *Journal
of the Atmospheric Sciences, 44*(12), 1559-1573.

Gómara, I., Pinto, J. G., Woollings, T., Masato, G., Zurita-Gotor, P., &
Rodríguez-Fonseca, B. (2014). Rossby wave-breaking
analysis of explosive cyclones in the Euro-Atlantic sector.
*Quarterly Journal of the Royal Meteorological Society,
140*(680), 738-753.

Hawcroft, M. K., Shaffrey, L. C., Hodges, K. I., & Dacre, H. F.
(2012). How much Northern Hemisphere precipitation is
associated with extratropical cyclones? *Geophysical
Research Letters, 39*(24),
https://doi.org/10.1029/2012GL053866.

Hodges, K. (1994). A general-method for tracking analysis and its
application to meteorological data. *Monthly Weather
Review, 122*(11), 2573-2586

Hodges, K. (1995). Feature tracking on the unit sphere. *Monthly
Weather Review, 123*(12), 3458-3465.

Hodges, K. (1999). Adaptive constraints for feature tracking.
Monthly Weather Review, 127(6), 1362-1373.

Hoskins, B. J., McIntyre, M. E., & Robertson, A. W. (1985). On the
use and significance of isentropic potential vorticity
maps. *Quarterly Journal of the Royal Meteorological
Society, 111*(470), 877-946.

Hoskins, B. J., & Hodges, K. I. (2002). New perspectives on the
Northern Hemisphere winter storm tracks. *Journal of the
Atmospheric Sciences, 59*(6), 1041-1061.

Kang, J. M., Lee, J., Son, S. W., Kim, J., & Chen, D. (2019). The
rapid intensification of East Asian cyclones around the

Korean Peninsula and their surface impacts. *Journal of Geophysical Research: Atmospheres*. https://doi.org/10.1029/2019JD031632.

Lee, J., Son, S. W., Cho, H. O., Kim, J., Cha, D. H., Gyakum, J. R., & Chen, D. (2020). Extratropical cyclones over East Asia: climatology, seasonal cycle, and long-term trend. *Climate Dynamics*, *54*(1-2), 1131-1144.

Seiler, C. (2019). A Climatological Assessment of Intense Extratropical Cyclones from the Potential Vorticity Perspective. *Journal of Climate*, *32*(8), 2369-2380.

Stoelinga, M. T. (1996). A potential vorticity-based study of the role of diabatic heating and friction in a numerically simulated baroclinic cyclone. *Monthly Weather Review*, *124*(5), 849-874.

Tamarin, T., & Kaspi, Y. (2016). The poleward motion of extratropical cyclones from a potential vorticity tendency analysis. *Journal of the Atmospheric Sciences*, *73*(4), 1687-1707.

Wang, C. C., & Rogers, J. C. (2001). A composite study of explosive cyclogenesis in different sectors of the North Atlantic. Part I: Cyclone structure and evolution. *Monthly Weather Review*, *129*(6), 1481-1499.

Yoshida, A., & Asuma, Y. (2004). Structures and environment of explosively developing extratropical cyclones in the northwestern Pacific region. *Monthly Weather Review*, *132*(5), 1121-1142.
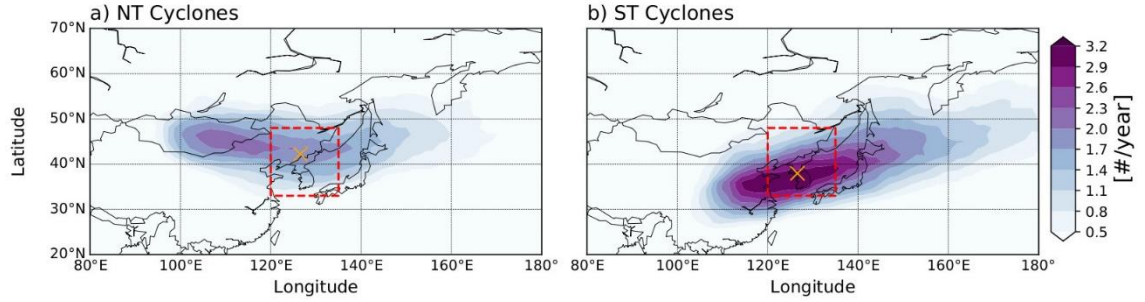
8. Figures

Figure 1. Track frequency (shading, ETC track points within 555 km radius from each grid point, units: number per year) of (a) NT and (b) ST cyclones. The average locations of the cyclones at their t_{max} are denoted with yellow X.
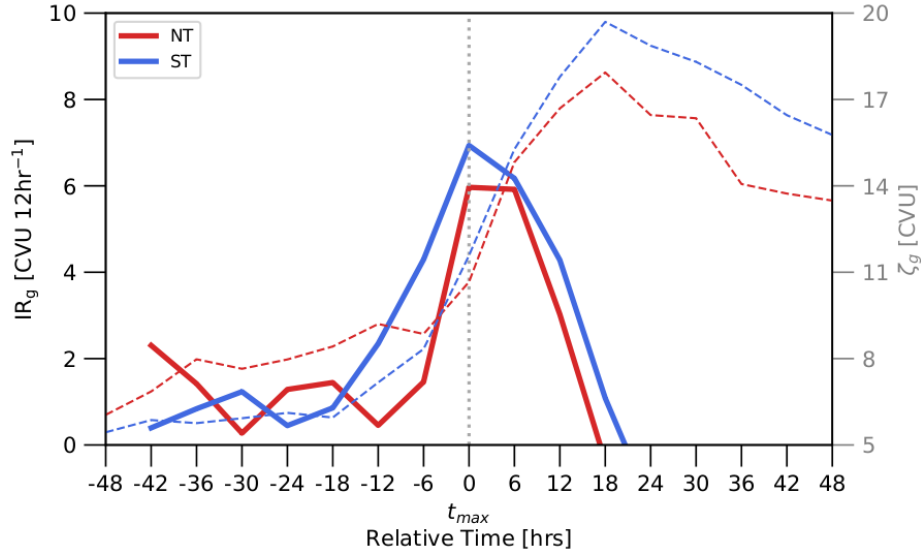
Figure 2. Temporal evolution of (solid, left axis, units: CVU 12hr^{-1}) IR_g and geostrophic vorticity (dashed, right axis, units: CVU 12hr^{-1}) of (red) NT and (blue) ST cyclones with respect to $t_{\max}$.
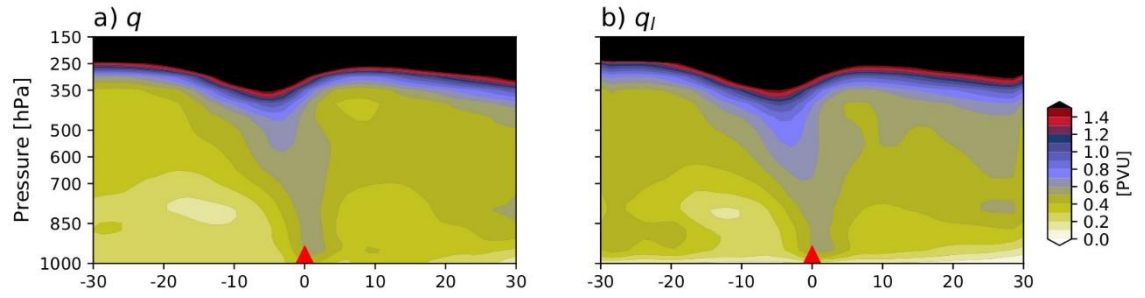
Figure 3. Vertical cross-section of (a) PV and (b) LPV (shading, units: PVU) with respect to the center of both NT and ST cyclones (red triangle) at t_{max}.
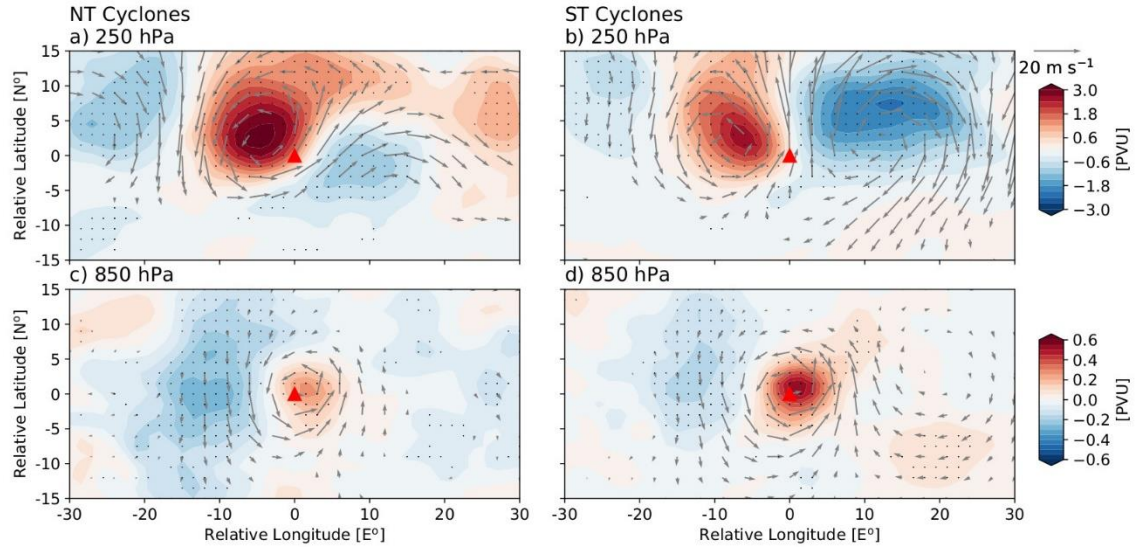
Figure 4. (a) LPV and wind anomalies at 250 hPa with respect to the center of NT cyclones (red triangle) at t_{max}. (b) Same as (a), but for ST cyclones. (c,d) Same as (a,b), but at 850 hPa. The LPV anomalies that are statistically significant at the 95% confidence level, based on two−tailed Students t−test, are dotted. Only wind anomalies that are equally significant are depicted.
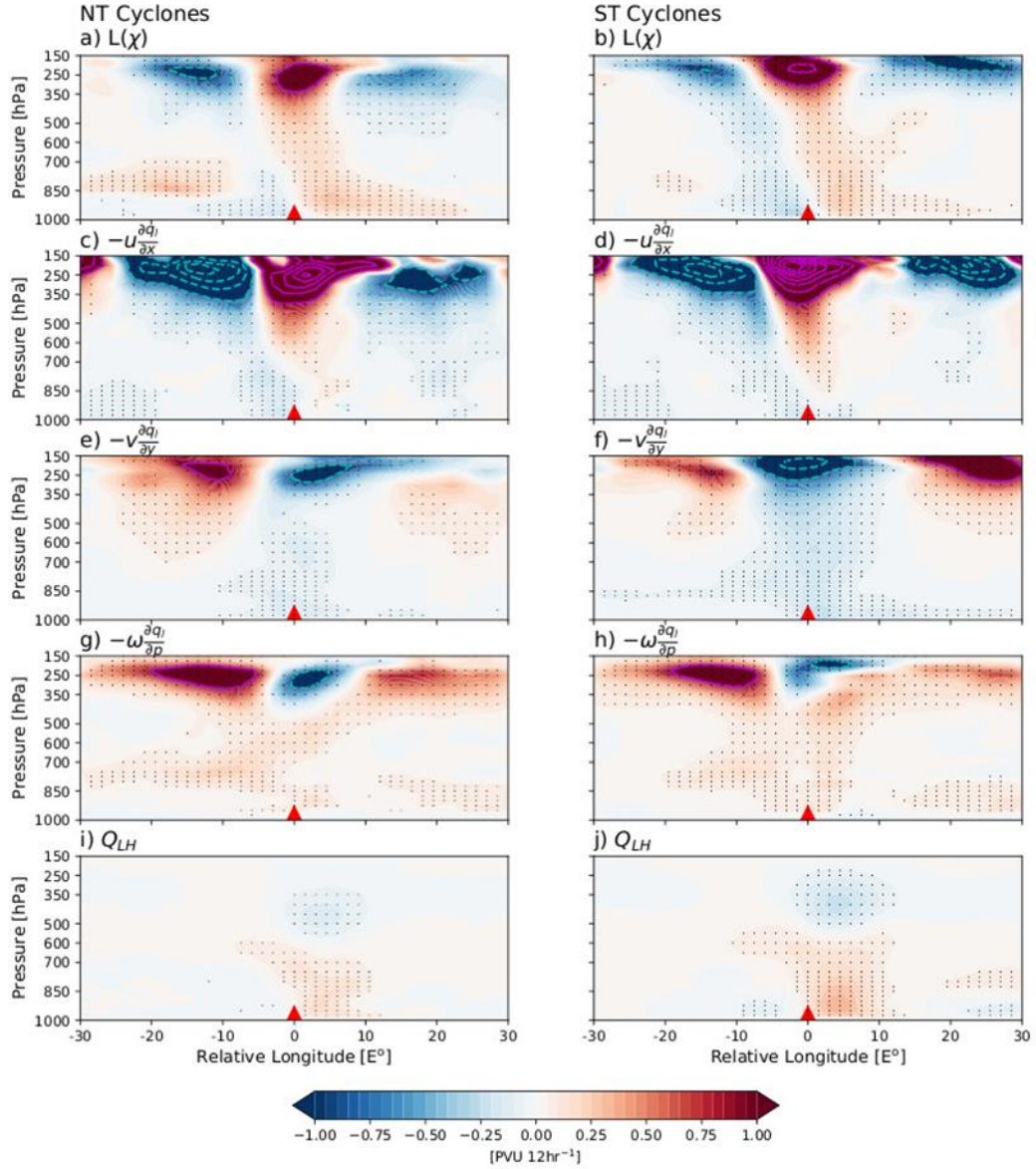
Figure 5. Vertical cross-section of (a, b) $\mathrm{L}(\chi)$, (c,d) $-u\frac{\partial q_L}{\partial x}$, (e,f) $-v\frac{\partial q_L}{\partial y}$, (g,h) $-\omega\frac{\partial q_L}{\partial p}$, and (i,j) Q_{LH} (shading, units: PVU 12 hr^{-1}) with respect to the center of NT and ST cyclones (red triangle) at $t_{\max}$. The values that are statistically significant at the 95% confidence level, based on the Bootstrap resampling test, are dotted.
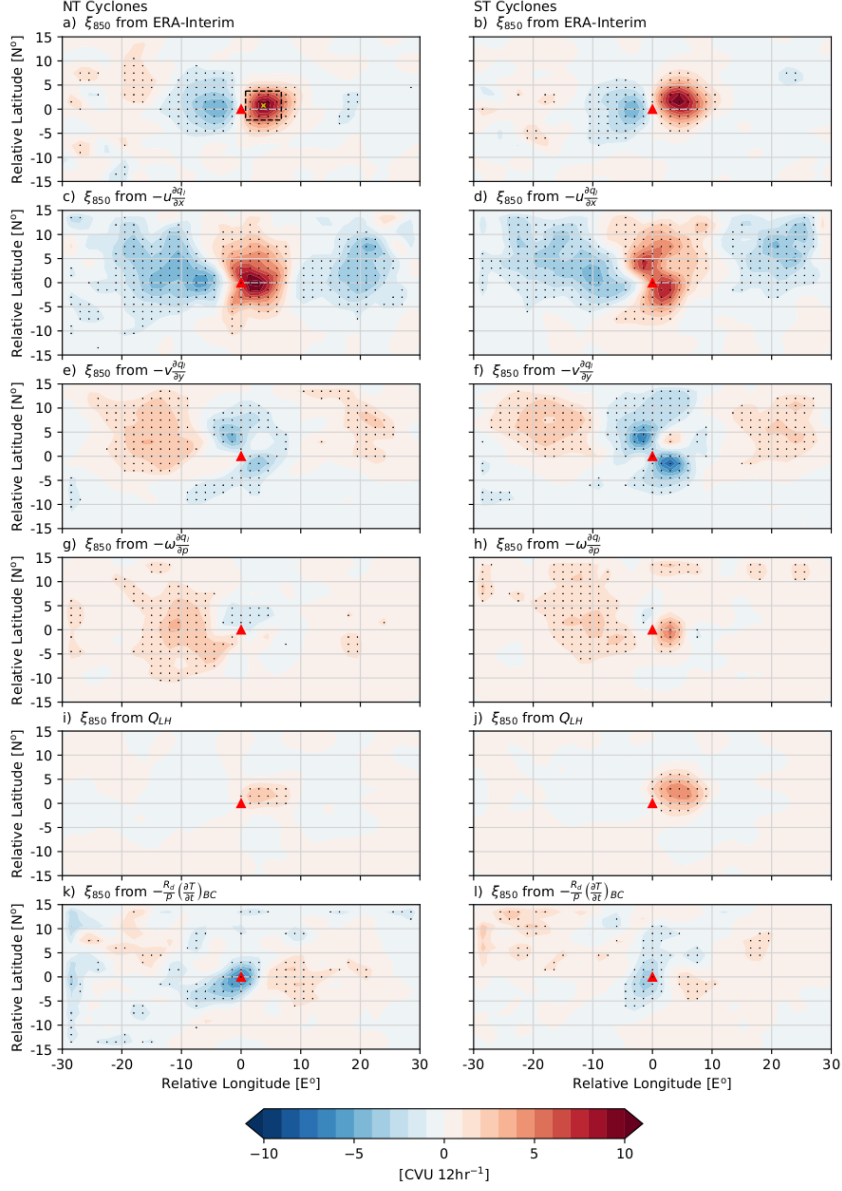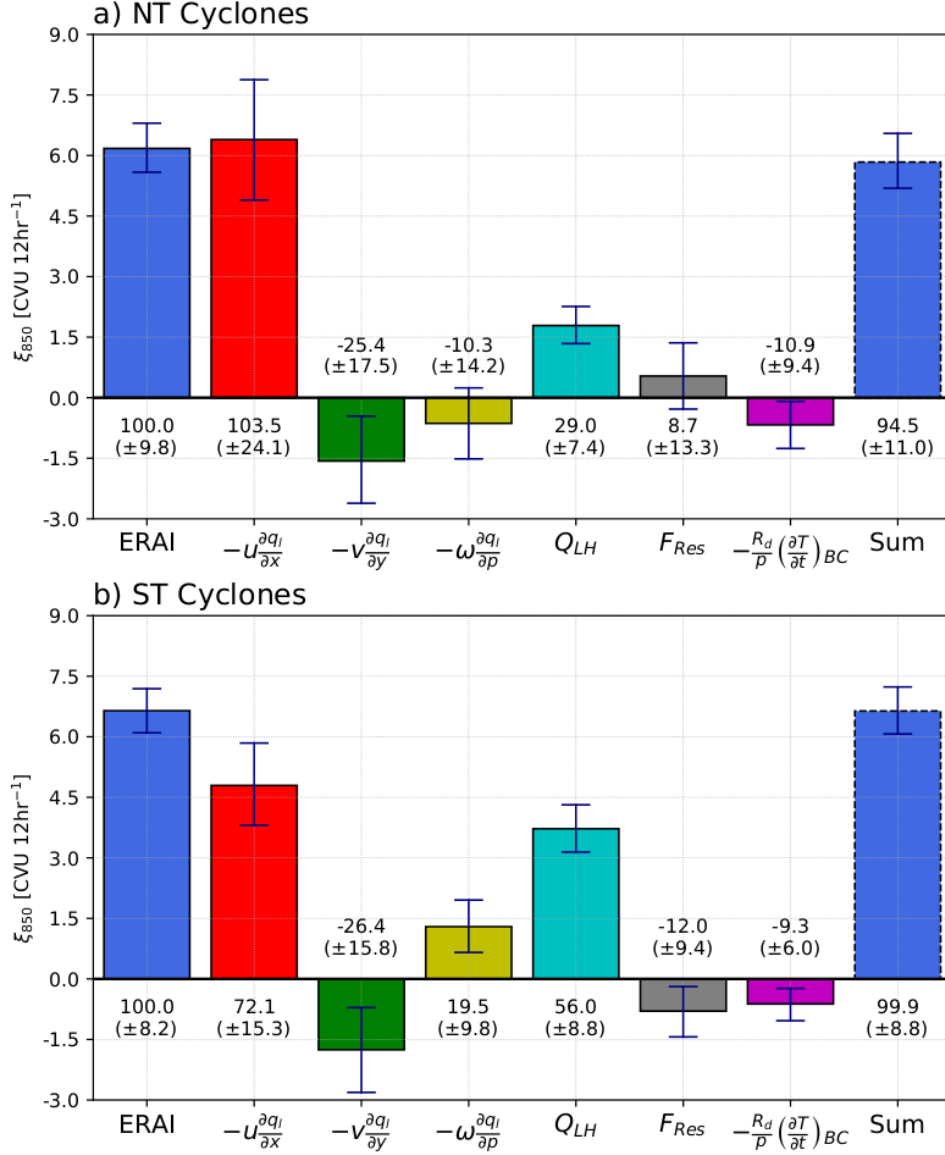
Figure 6. ξ_{850} from (a, b) reanalysis, (c,d) $-u\frac{\partial q_l}{\partial x}$, (e,f) $-v\frac{\partial q_l}{\partial y}$, (g,h) $-\omega\frac{\partial q_l}{\partial p}$, (i,j) Q_{LH}, and (k, l) $-\frac{R_d}{p}\left(\frac{\partial T}{\partial t}\right)_{BC}$ (shading, units: CVU 12 hr^{-1}) with respect to the center of NT and ST cyclones (red triangle) at t_{max}. The values that are statistically significant at the 95% confidence level, based on the Bootstrap resampling test, are dotted.

Figure 7. Area-averaged ξ_{850} for reanalysis, inversions and the sum of piecewise inversions for (a) NT and (b) ST cyclones. The relative contribution to observed ξ_{850} (leftmost bar) is denoted in percentage. The 95% confidence intervals, based on the Bootstrap resampling test, are also shown. The 95% confidence intervals, based on the Bootstrap resampling test, are also shown.
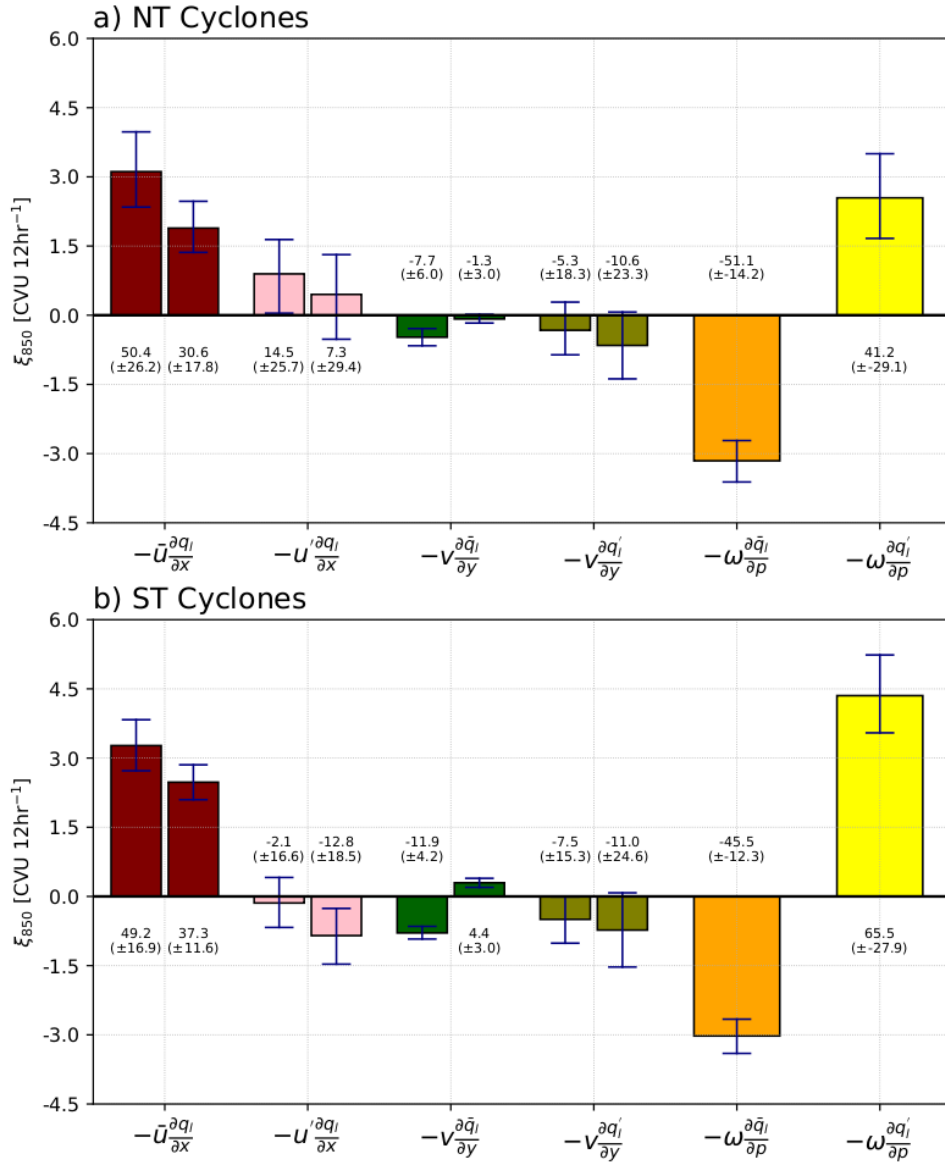
Figure 8. Same as Fig. 7, but for decomposed advection terms.
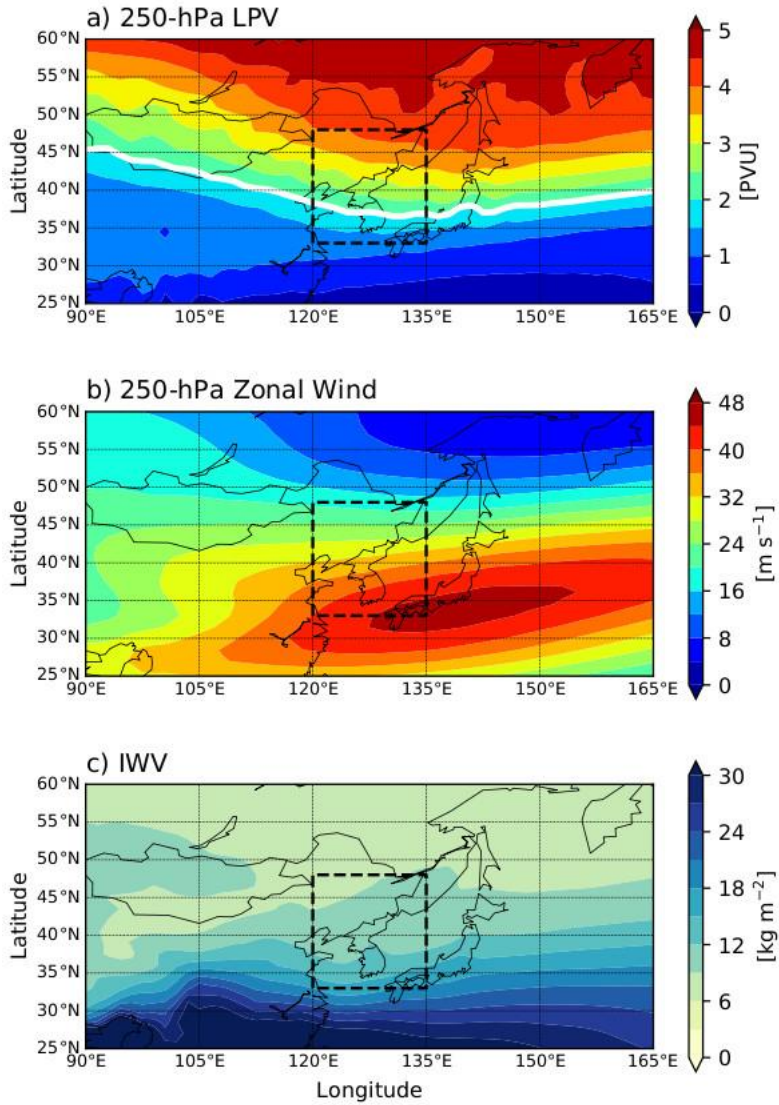
9. Supplementary Figures

Figure S1. Springtime (March–May) climatology of (a) LPV (shading, units: PVU) and (b) zonal wind (shading, units: m s^{-1}) at 250 hPa, and (c) integrated water vapor from 1000 to 250 hPa (shading, units: kg m^{-2}). In (a) the 2–PVU line is depicted in white as a reference.
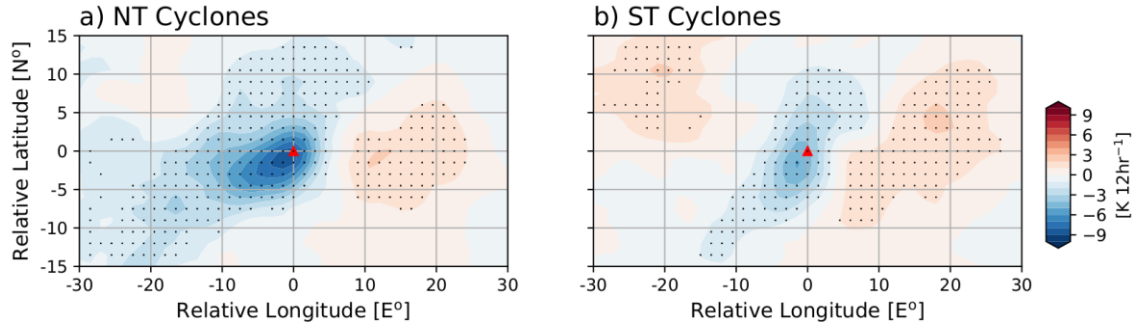
Figure S2. Temperature tendency at 875 hPa (shading, units: K 12hr^{-1}) with respect to the center of (a) NT and (b) ST cyclones at t_{max}. The values that are statistically significant at the 95% confidence level, based on Bootstrap resampling test, are dotted.
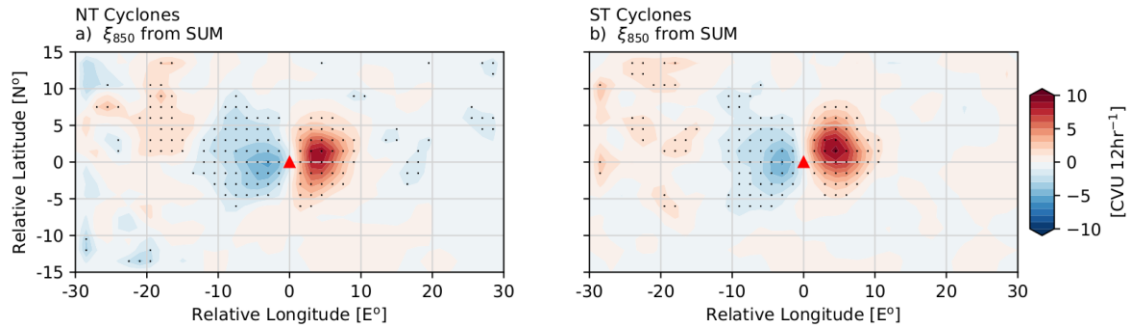
Figure S3. Same as Fig. 6 but for ξ_{850} from sum of piecewise inversions.

국문 초록

한반도 근처 저기압의 발달 과정

강준석
지구환경과학부
석사과정
서울대학교

본 연구에서는 한반도 근처 동아시아 급격히 발달하는 저기압의 발달과 정을 잠재와도 경향 방정식 인버전을 통해 정량적으로 분석한다. 한반도 근처에서 급격히 발달하는 저기압은 몽골지역에서 발생하는 북쪽 트랙과 동중국지역에서 발생하는 남쪽 트랙으로 나뉜다. 북쪽 트랙 저기압들의 경우 잠재와도의 동서방향 이류(103.5%)와 잠열 방출(29.0%)에 의해 서 급격하게 발달한다. 남쪽 트랙 저기압 또한 두 과정(각각 72.1%와 56.0%)에 의해 급격하게 발달하고 잠재와도의 연직 이류(19.5%)에 의해서도 강화된다. 잠재와도의 남북방향 이류($\sim-25\%$)와 지표 온도 경향 (-10%)은 두 트랙의 저기압들의 발달을 저해한다. 이류항들을 추가 적으로 분해하여 각 저기압 트랙 별 이류항의 기여도 차이의 원인을 분석하였다. 두 트랙에서 나타난 동서방향 이류의 차이는 대류권 상층 골의 축과 관련이 있다. 잠열 방출항의 차이는 하층 잠재와도 생성에 차이를 일으켜 연직 이류의 기여도의 차이도 발생시킨다.

주요어: 동아시아 저기압, 온대저기압 발달 과정, 한반도, 잠재와도, 잠재와도 경향 방정식, 잠재와도 인버전
학번: 2018−27970